New Journal of Physics
The open-access journal for physics

Realization of optical superlens imaging below the diffraction limit

Hyesog Lee, Yi Xiong, Nicholas Fang, Werayut Srituravanich, Stephane Durant, Muralidhar Ambati, Cheng Sun and Xiang Zhang
5130 Etcheverry Hall, Center for Scalable and Integrated Nanomanufacturing (SINAM), University of California, Berkeley, CA 94720, USA
E-mail: xiang@berkeley.edu

New Journal of Physics **7** (2005) 255
Received 30 August 2005
Published 19 December 2005
Online at http://www.njp.org/
doi:10.1088/1367-2630/7/1/255

Abstract. Recently, the concept of superlensing has received considerable attention for its unique ability to produce images below the diffraction limit. The theoretical study has predicted a 'superlens' made of materials with negative permittivity and/or permeability, is capable of resolving features much smaller than the working wavelength and a near-perfect image can be obtained through the restoration of lost evanescent waves (Pendry 2000 *Phys. Rev. Lett.* **85** 3966–9). We have already demonstrated that a 60 nm half-pitch object can indeed be resolved with $\lambda_0/6$ resolution with the implementation of a silver superlens with $\lambda_0 = 365$ nm illumination wavelength, which is well below the diffraction limit (Fang *et al* 2005 *Science* **308** 534–7). In order to further support the imaging ability of our silver superlens, a two-dimensional arbitrary object with 40 nm line width was also imaged (Fang *et al* 2005 *Science* **308** 534–7). In this paper, we present experimental and theoretical investigations of optical superlensing through a thin silver slab. Experimental design and procedures as well as theoretical studies are presented in detail. In addition, a new superlens imaging result is presented which shows the image of a 50 nm half-pitch object at $\lambda_0/7$ resolution.

1367-2630/05/010255+16$30.00
PII: S1367-2630(05)06843-6

Contents

1. Introduction

Conventional optical imaging systems, such as optical microscopes, produce the image of an object in the far field by collecting the scattered propagating waves. A major setback of such imaging methods is the loss of evanescent components at the image plane; the intensity exponentially decreases along the optical path within order of the wavelength of light. The absence of evanescent waves which carry sub-wavelength information results in the diffraction limit, a fundamental limitation on the smallest resolvable feature size, which is about half of the working wavelength ($\lambda/2$). Contact mask imaging is one of the early efforts that has been explored to minimize the evanescent decay [1]. Immersion microscopy improves the resolution by increasing the refractive index of the surrounding medium ($\lambda_0/2n$), where λ_0 is free space wavelength, but there is a limited availability of high-refractive index materials in nature. A near-field scanning optical microscopy (NSOM) brings an optical fibre with a sharp tapered end in the vicinity of an object for imaging sub-wavelength features, but it suffers from slow speed of serial scanning [2].

Recently, Pendry predicted [3] the possibility of diffraction-free imaging by a flat slab lens made of 'left-handed material' (LHM), a material with negative permittivity and negative permeability as termed first by Veselago [4]. This remarkable perfect imaging is possible because Pendry's 'Perfect Lens' not only focuses propagating waves just as normal lenses do, but it also amplifies evanescent waves [3]; all orders of diffracted propagating waves and evanescent waves can be collected at the image plane. Smith and co-workers experimentally demonstrated for the first time Veselago's original idea of negative refraction in microwave region [5]. Unprecedented electromagnetic properties of artificial metamaterials in the microwave and terahertz (THz) regime have been demonstrated [5]–[14]. However, there is no known LHM in the optical region to function as a true optical superlens partly because of the diminishing magnetic response of nature materials in optical frequency. THz magnetic responses have only recently been realized [6, 11]. However, in optics it is well known that the electric field and the magnetic field decouple in the quasi-static limit which can be utilized for near-perfect lensing, in which case only negative permittivity is required to realize such 'superlensing' in near field [3]. Numerical studies have already shown that superlensing via a thin silver slab with remarkable resolution is indeed possible [3], [15]–[17].

In this paper, we present an experimental as well as a corresponding numerical study of optical superlensing through the amplification of evanescent field. A thin slab of silver is chosen as the superlens which has a negative permittivity at a wavelength of 365 nm [18]. The

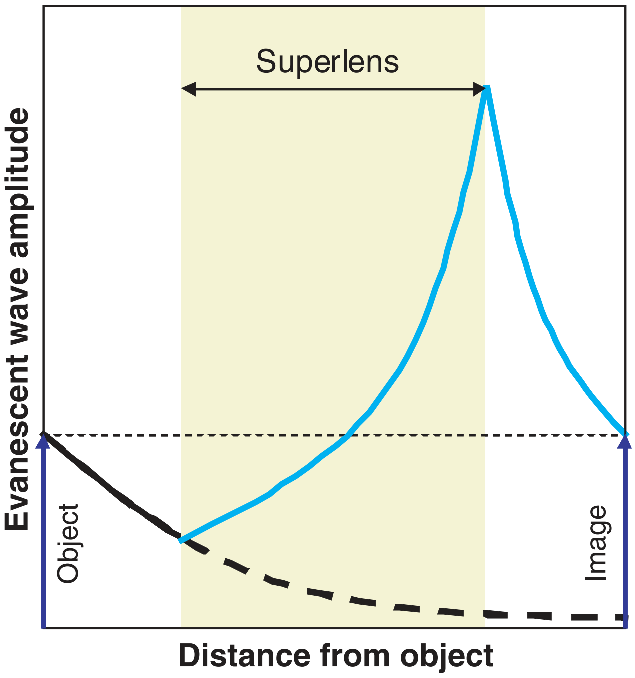

Figure 1. Principle of superlensing. The black curve shows the decay of evanescent wave in positive refractive index materials such as dielectrics. The blue curve shows the enhancement of evanescent waves by a superlens, which decays again on the other side restoring the original amplitude at the image plane. The black dotted curve represents a decaying field without a superlens [25, 29].

evanescent component of the wave scattered by the object is significantly amplified (figure 1) due to surface plasmon (SP) excitation—collective oscillation of free electrons at the interface of a dielectric and a conducting medium [19, 20]. This can be achieved by closely matching the permittivity of the silver slab and the surrounding environment, allowing the P-polarized portion of the scattered light to excite SP waves at the silver surface [3]. Recent experiments confirmed the evanescent field enhancement through a silver film, a key precursor for the superlens [21, 22]. Further confirmed by recent experimental studies is the ability of imaging through a thin silver film with the resolution up to $\lambda_0/6$ by Fang *et al* [23].

We show in this paper, through detailed numerical studies and experiments, that a carefully designed superlens can indeed image sub-wavelength features with resolution significantly higher than the diffraction limit. In the subsequent sections, the design of the superlensing experiment is presented, followed by numerical simulations for the optimization of the sample configuration. After detailed sample fabrication and experimental procedures are presented, the imaging results are discussed.

2. Design of the superlens experiment

The superlens is in the form of a thin slab of metal. Sub-wavelength objects are to be imaged through the superlens recorded on the opposite side in photoresist (PR). The key to the experiment design is to carefully select the working wavelength and the thickness of the slab in order to maximize the enhancement of evanescent waves.

Among noble metals that exhibit negative permittivity in optical frequency, silver was chosen as the superlens material for its low-absorption loss. Due to the strong dispersive behaviour of metals, the selection of illumination wavelength (λ_0) is critical to the superlens design. $\lambda_0 = 365$ nm is used in the experiment for two main reasons. The relative permittivity of silver (ε_{m}) is negative ($\varepsilon_{\mathrm{m}} = -2.4012 + \mathrm{i}0.2488$ at 365 nm) [18], and its real part matches closely with that of the surrounding dielectric material, polymethyl-metacrylate (PMMA, $\varepsilon_{\mathrm{d1}} = 2.301$ at 365 nm), for wide SP band excitation [24].

On the other side of the slab, an i-line negative PR (NFR 105G, Japan Synthetic Rubber Microelectronics (JSR Micro)) with relative permittivity $\varepsilon_{\mathrm{d2}} = 2.886 + \mathrm{i}0.059$ was directly spun on for image recording. Even though there is a slight mismatch of $\varepsilon_{\mathrm{d1}}$ and $\varepsilon_{\mathrm{d2}}$, it is numerically shown that such an asymmetric lossy superlens still supports the efficient coupling of the evanescent fields between two surfaces of the silver film [25]. In addition, the 365 nm source is readily available from the i-line of the mercury arc lamp spectrum as it is widely used in photolithography processing.

The enhancement of the evanescent field strongly depends on the thickness of silver and PMMA layers. Numerical analysis of thickness dependent optical transfer functions are shown in figure 2. Transmissivity of P-polarized waves ($|\mathrm{Tp}|^2$) scattered by the object is plotted using Fresnel equations for multi-layer structures. The superlens structure, PMMA/silver/PR, with infinitely thick PR is considered while the thicknesses of PMMA and silver are varied. In figure 2(a), the silver thickness is varied from 15 to 55 nm with fixed PMMA thickness of 40 nm, and the 35 nm silver slab gives the optimum transfer function with resolution limit up to $4k_0$. Thinner sliver slabs, 15 and 25 nm, show higher but narrow enhancement bands. Thicker slabs of 45 and 55 nm show smaller enhancements in reference to zero-order transmission, which results in low image contrast of sub-diffraction-limited features. In figure 2(b), PMMA thickness is varied from 30 to 60 nm, while the silver thickness is held at 35 nm. As expected, thinner PMMA shows larger enhancements.

Figure 2(c) shows thickness-dependent transmissivity for one particular wavenumber, $2\pi/120$ nm, with varying silver thickness. Due to the competition between SP resonance and intrinsic loss in the metal, an optimum thickness—35 nm in this case—exists for maximum field enhancement across a silver slab [21, 26]. Improper thickness often leads to diminishing the enhancement resulting in a diffraction-limited image [27]. Finally, figure 2(d) shows polarization dependence of evanescent field enhancement through the designed structure; 40 nm of PMMA, 35 nm of silver and thick PR layer (>100 nm). The choice of 40 nm PMMA came from difficulties in fabrication. As further discussed in a later section, it is a challenging task to planarize such a thin layer of PMMA on a Cr grating object with 50 nm groove depth. Afterwards, the incident light is scattered by an object. Only transverse magnetic (TM) component waves can excite SPs on the silver surface. The blue curve shows enhanced transmission through the superlens with TM incident waves and the red curve is that of transverse electric (TE) waves where there is no enhancement. Also shown is the transfer function of the control structure, where silver is replaced with a dielectric PMMA layer of the same thickness. As expected, the evanescent waves decay strongly without a silver layer even with TM incident waves (dotted line). Following the numerical analysis and design, an experiment was carried out to demonstrate superlensing by imaging an object through a silver slab below the diffraction limit.

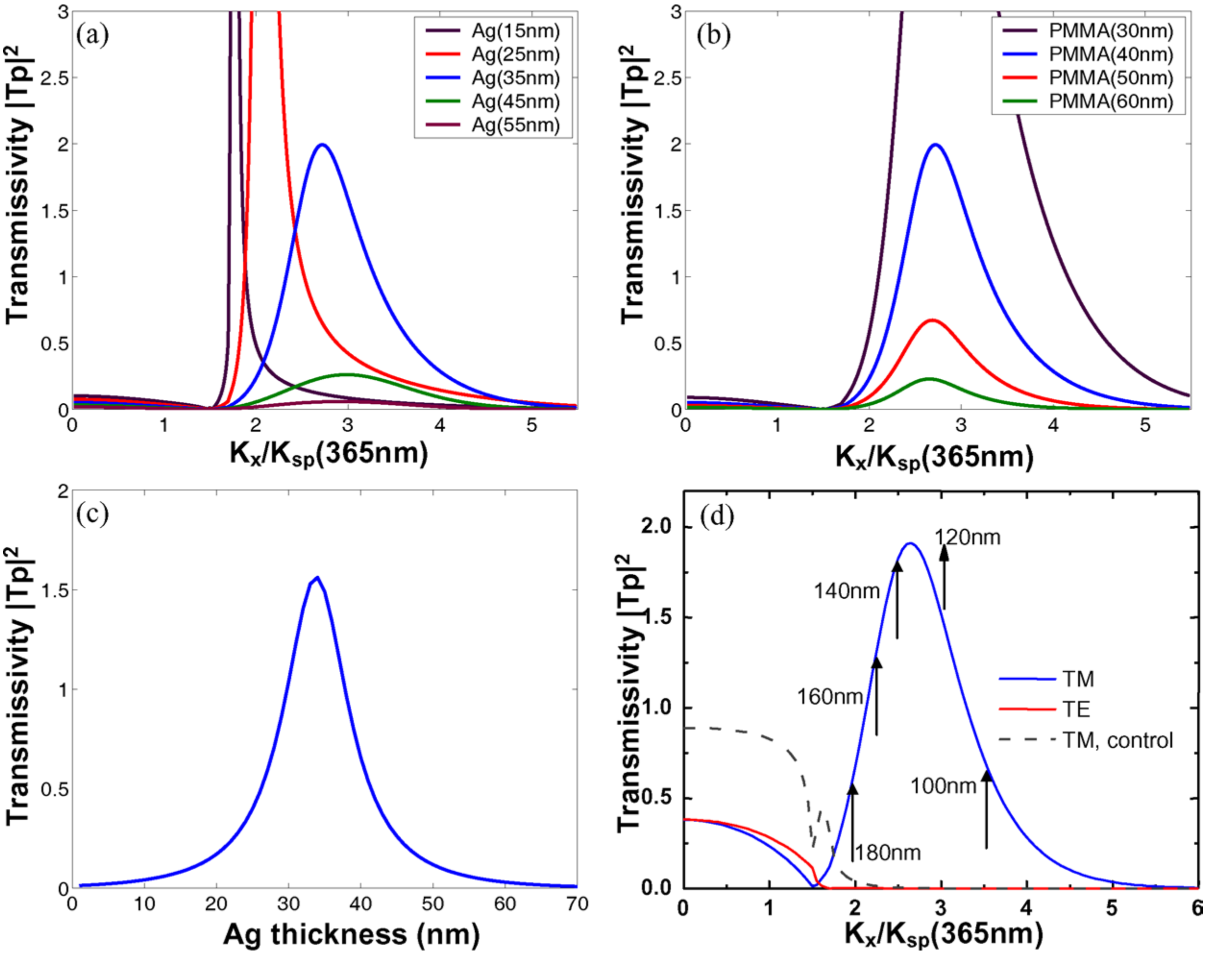

Figure 2. Numerical study on the transmissivity of various superlens structure configurations. (a) PMMA thickness fixed at 40 nm and silver thickness varying from 15 to 55 nm in 10 nm step. (b) Silver thickness fixed at 35 nm and PMMA thickness varying from 30 to 60 nm in 10 nm step. (c) Transmissivity of one wavenumber, $2\pi/120\,\text{nm}$, with varying silver thickness from 0 to 70 nm in 1 nm step. PMMA thickness is fixed at 40 nm. (d) Polarization-dependent transmissivity through a superlens structure (PR/Silver (35 nm)/PMMA (40 nm)) and a control structure (PR/PMMA (75 nm)) [23]. TM polarization shows enhancement through a superlens structure, while the TE polarized component through the superlens structure and the TM components in the control sample show strongly attenuated transmissivity of evanescent waves.

Figure 3(a) shows the superlens sample structure with designed PMMA and silver thicknesses of 40 and 35 nm, respectively. This asymmetric configuration takes advantage of translation symmetry ($di + ds = w$ where, di is object–silver distance, ds is silver–image distance, and w is the thickness of the silver slab). As di is still greater than w, imaging is performed directly on the silver surface to harness the maximum field enhanced by the silver slab [16]. A sub-wavelength object—Cr nanowire grating with sub-wavelength period (120 m)—is located on one side of the silver slab. After the object scatters normal incident light at 365 nm, evanescent waves

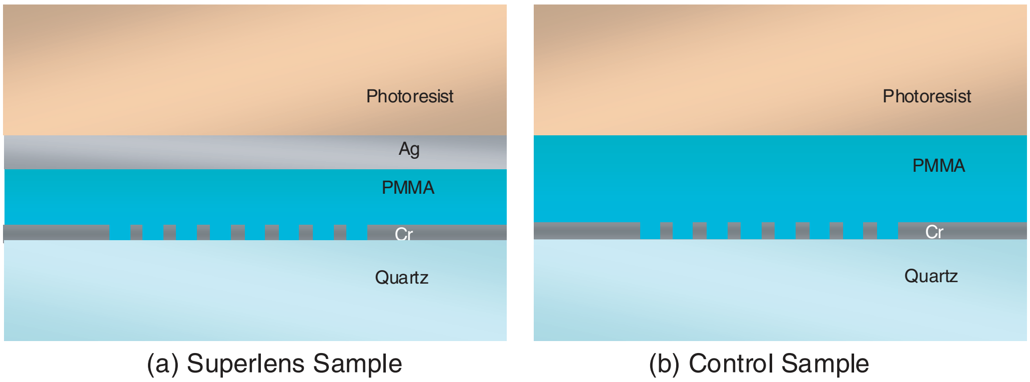

Figure 3. (a) Cross-section of the superlens sample structure. A sub-wavelength Cr grating object with 120 nm period is fabricated on quartz substrate using a Focused Ion Beam and planarized with 40 nm thick PMMA. Then 35 nm silver layer is deposited through E-beam evaporation and 120–150 nm PR is spun on as the imaging medium. The sample is exposed using the i-line (365 nm) of a mercury lamp and the superlensing image is recorded by PR. (b) Cross-section of the control sample structure. The same imaging method is used on 75 nm of a planarized PMMA layer.

are generated and the P-polarized waves excite SPs at silver/PMMA interface. The evanescent field is then significantly enhanced and coupled with that of the other side of the silver layer. Then, the original field of the object is restored which is recorded by PR. While it is possible to image a grating object by restoring a narrow band of Fourier components, it is necessary to excite a wide band of large wavenumbers in order to image an arbitrary object with sub-diffraction-limited resolution. From figure 2(a), it can be determined that wavenumbers in the range, $2k_0 \sim 4k_0$, can be transmitted through the superlens [23], and an arbitrary line object, 'NANO', with line width of 40 nm, which consists of a broad band of Fourier components, was sucessfully imaged in this experiment, which will be further discussed in a later section. In the structure (figure 3(b)), the 35 nm silver layer was replaced by a 35 nm PMMA layer, totalling the thickness of PMMA to 75 nm. It is designed to prove that the enhancement of evanescent waves and subsequent optical superlensing is not possible without the silver slab.

Although our numerical calculations using Fresnel equations provide insightful information on the field transmission through the superlens structure, additional parameters, such as material properties of the object (Cr) and possible multiple reflections between the object and superlens, also needs to be considered. Therefore, full vector simulation software (Microwave Studio, CST) has been used to simulate the imaging for a grating object with 120 nm period (figure 4). The periodic boundary conditions were applied. The simulated E-field distribution for our superlens sample structure is shown in figure 4(a). The sample consists of 50 nm Cr grating objects, 40 nm PMMA spacer layer, 35 nm silver layer, and a thick layer of PR. The image of 120 nm period formed in the PR layer can be clearly resolved. For comparison, the E-field intensity distribution for two control configurations have also been simulated (see figures 4(b) and (c)). By removing the silver layer, the E-field distribution at 40 nm away from Cr object has been shown in figure 4(b). The results exhibit significant reduction of the field contrast as the indication of diminishing evanescent field. Similar results can also be found in another control configuration,

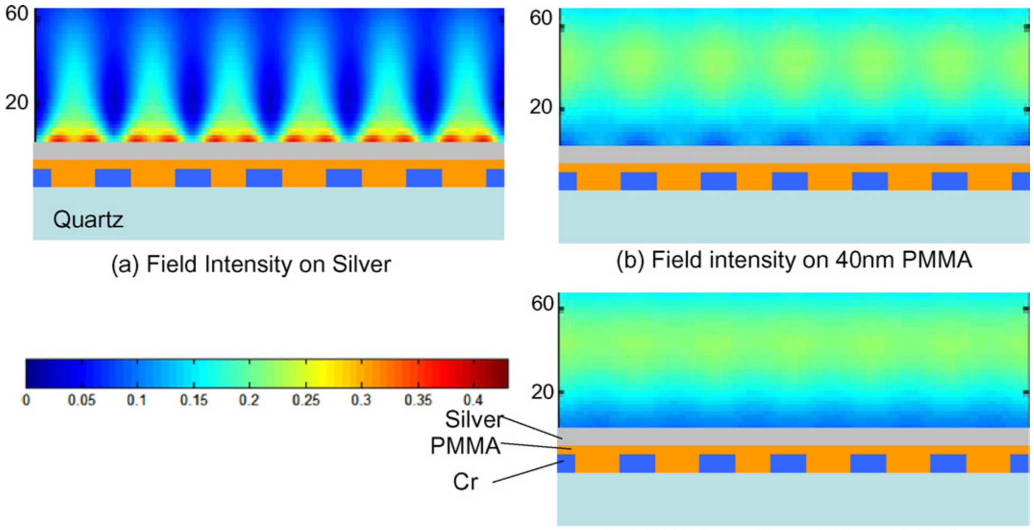

(a) Field Intensity on Silver

(b) Field intensity on 40nm PMMA

(c) Field intensity on 75nm PMMA

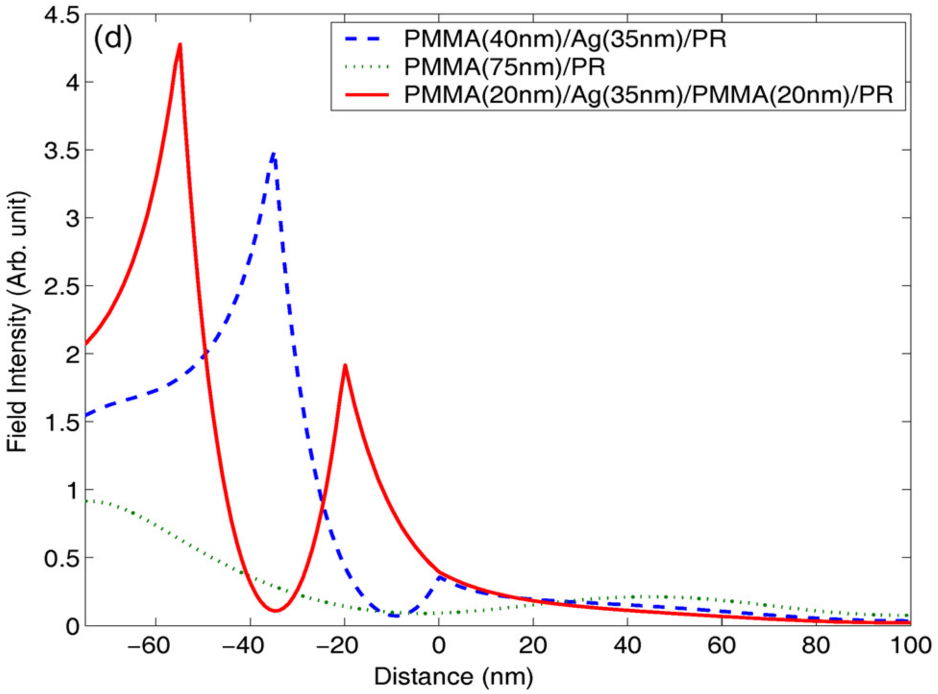

Figure 4. Simulated total E-field intensity profiles in the PR layer located above (a) 35 nm silver superlens, (b) and (c) PMMA layers with 40 nm and 75 nm thickness respectively. Six periods are simulated with periodic boundary conditions. The placement of 35 nm silver superlens amplifies the field while further attenuation is resulted when additional 35 nm of PMMA layer was placed above 40 nm PMMA. (d) Simulated E-field intensity distribution obtained using superlens structure (PMMA (40 nm)/Ag (35 nm)/PR) and the symmetric sample configuration structure (PMMA (20 nm)/Ag (35 nm)/PMMA (20 nm)/PR) exhibit intensity peaks at both interface of the silver slab. The control structure (PMMA (75 nm)/PR) shows continuous decay of the field as expected.

where 35 nm silver film has been replaced by a PMMA layer with the same thickness. Comparing with the case shown in figure 4(b), the added 35 nm thickness of the PMMA layer simply causes additional decay of the evanescent field, resulting in even poorer contrast. These results provide strong evidence of enhanced transmission of evanescent field using silver superlens, which is capable of imaging beyond the diffraction limit. To justify our design of asymmetric sample configuration due to fabrication difficulties, we also performed numerical simulation to compare with the symmetric configuration. The cross-section of the E-field distribution was obtained along the centre line of the grating opening for the superlens structure (PMMA (40 nm)/Ag (35 nm)/PR) and the symmetric structure (PMMA (20 nm)/Ag (35 nm)/PMMA (20 nm)/PR), and are shown in figure 4(d) as blue and red lines, respectively. The E-field strengths are comparable at PR interface ($x = 0$) for both configurations, which validates the use of asymmetric configuration in this experiment. The E-fields maximum at both surface of silver are indications of SP excitation [17, 25]. The profile of the control structure (PMMA (75 nm)/PR) shows continuous decay as expected, while the small peak near the position at $x = 50$ nm is believed to be due to the field reflected from the boundary of the simulation domain.

3. Fabrication and experiment procedures

The fabrication process of the superlens sample shown in figure 3(a) starts with an ultraviolet (UV) transparent quartz wafer. A 50 nm thick Cr layer is deposited using E-beam evaporation (SLOAN), and the objects are fabricated on the Cr film by Focused Ion Beam (Strata, FEI Company). Line gratings as well as a two-dimensional line pattern, 'NANO' were written with a line width of ∼40 nm. The periods of grating objects range from 100 to 180 nm in 20 nm step with 60 nm line width. Figures 5(a) and (b) show atomic force microscopy (AFM) surface profiles of a grating object with 120 nm periods. Then a 40 nm thick planarized spacing layer is applied on the object layer (figures 5(c) and (d)) using PMMA, followed by the deposition of a 35 nm silver layer by E-beam evaporation (figures 5(e) and (f)). The silver surface is coated with negative PR (NFR105G, JSR Micro) and is exposed from the substrate side to record the image reconstructed by the superlens.

The planarization of the spacing layer is a crucial step in our sample fabrication because imperfect surface conditions of the silver layer will modify its dispersion relation, which limits the final resolution [15]. The spacing layer needs to eliminate the surface modulation inherent from Cr objects and its surface needs to be smooth enough—down to 1 nm in root mean square (RMS)—in order to minimize the surface roughness of silver. SiO_2 was the first choice for the spacing layer material. It was deposited by e-beam evaporation, and chemical mechanical polishing (CMP) was used to flatten the surface. However, this process yielded inconsistent surface quality and difficulty in thickness control due to unstable CMP parameters. With PMMA, stable processes were developed that can reduce the modulations of the object to less than 1 nm and give better control of the thickness of the film. According to the superlens structure design discussed in previous section, it is desirable to have the spacing layer as thin as possible. However, it is found that the film quality degrades when it is thinner than 40 nm. Such a thin layer with desirable flatness on 50 nm deep gratings is not achievable with a single-spin coating process because the polymer layer tends to follow the profile of the surface topology [28].

In order to achieve a 40 nm thick planarized and smooth PMMA layer, firstly, multiple spin coatings of PMMA produce a thick layer (∼0.7 μm) which eliminates the surface irregularities

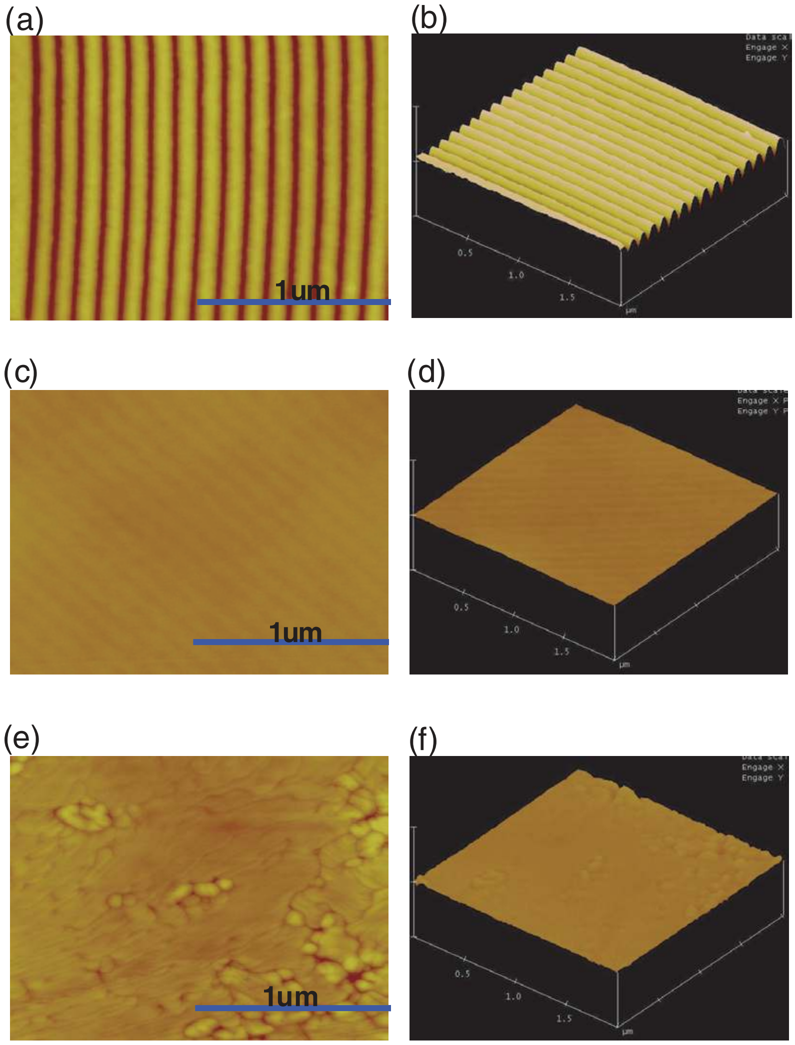

Figure 5. Surface profiles of each fabrication step imaged by AFM. (a) and (b) are the images of the grating object with 120 nm period; (c) and (d) planarized PMMA surface; and (e) and (f) silver surface. Even though the surface modulation inherent from the object reappears after the planarization on PMMA layer shown in (c) and (d), the object modulation is completely eliminated after the deposition of the silver layer shown in (e) and (f). (Colour scale: 0–100 nm).

of the object. The peak-to-valley is gradually reduced after each coat, and after several coatings, a flat surface is achieved. A sufficiently long bake (∼10 min on 180 °C hot plate) between each coating removes the solvent from the polymer and hardens the layer. Secondly, the desired thickness is achieved through oxygen plasma blanket etch. A commercial PR asher (Tegal) is used to etch PMMA down to 40 nm. Because of the nonlinear etch rate in the plasma, the thickness of PMMA film has to be monitored using Filmtek 2000 between short etching steps (∼1 min) to prevent over-etching. The typical etching rate for the first 2 min is 60–80 nm min^{-1} at 200 W, but the rate increases for longer etching as the chamber temperature increases. This etch-and-measure step is repeated until 40 nm thickness is reached. For the control sample, the etching stops when 75 nm thickness is reached. Finally, a reflow heating smoothes out the surface which was roughened by plasma bombardment during the blanket etch. Reflow effectiveness depends on the PMMA molecular weight and the flow temperature. The temperature has to be above the glass transition temperature (105 °C for PMMA) and be sufficiently high in order to induce effective surface flow of the heated fluid. Smaller molecules tend to have higher mobility when heated and readily smooth the roughened surface. However, if the temperature is too high, the cross-linking of the polymer chains hinders active movement of the molecules. Therefore, it is essential to find the optimal temperature for reflowing of PMMA. In our experiment, 495 PMMA is used and reflowed for 30 min at 180–200 °C on a hot plate. After planarization, less than 1 nm modulation and ∼0.5 nm RMS roughness have been achieved as shown in figures 5(c) and (d). It is noteworthy that the periodic modulation reappears after the reflow but it is small enough (∼1 nm peak-to-valley) for the designed experiment. Further studies are needed to verify the exact physics of this phenomenon.

On the planarized spacer layer, a 35 nm silver film was deposited using electron beam evaporation. The AFM image of the silver surface is shown in figures 5(e) and (f). The surface quality of the film has to be controlled in order to maximize the image quality [15]. Varying the deposition rate had significant effect on the surface quality of thin silver films. With the chamber pressure ($\sim 2.0 \times 10^{-6}$ torr) and the source weight held constant (∼60 g), the deposition rate was varied from 0.1 to 10 nm s^{-1}. Higher deposition rates produced better roughness of the silver surface while the grain size variation increased. Even though the average roughness analysis showed improvements—from 3–4 nm RMS at lower rate to 1–2 nm RMS at a higher rate—this is due to larger areas with lower roughness at higher deposition rate, not because the roughness of the entire surface homogeneously improved. Nevertheless, this increased the chance that the objects will be imaged on the flatter areas. The RMS roughness of the silver surface shown in figures 5(e) and (f) is ∼1.5 nm.

A negative tone i-line PR NFR 105G (JSR Micro) was used to record the image reconstructed by the superlens. As shown in figure 3, the i-line UV source is shone from the substrate side. Then, the object scatters the incident light producing evanescent waves. The P-polarized portion of the waves excites SPs at the silver/PMMA interface, and the enhanced and transmitted evanescent waves are recorded as an image on the other side of the slab. Diluted PR was spin-coated to approximately 120–150 nm thickness. Then, after 1 min of soft bake at 100 °C hotplate, the sample was exposed by 365 nm UV light on a commercial Karl Suss MA6 aligner. The post-exposure bake was 1 min at 100 °C and the image was developed. The developer was also provided by JSR Micro and diluted with de-ionized water with the ratio of 2 : 1 = developer : DI water. After an extensive parameter sweep of exposure and development conditions, 60 s exposure was used for superlensing imaging of the grating and ‘NANO’ object and the control imaging of ‘NANO’. 30 s exposure was used for the control imaging of grating objects. 15–60 s development time was enough for all experiments except for the control imaging of ‘NANO’ object, where longer than 2 min of development time produced no reduction of line width. The control experiments were carried out by replacing the silver layer with another layer of 35 nm thick PMMA film. With the original spacing layer thickness of 40 nm, the total thickness of PMMA in the control sample is 75 nm and a significant decay of the evanescent field is expected without the silver superlens. After the development and hard bake of the resist (∼1 min at 100 °C), the recorded topography was imaged by AFM (Dimension 3100, Digital Instrument).

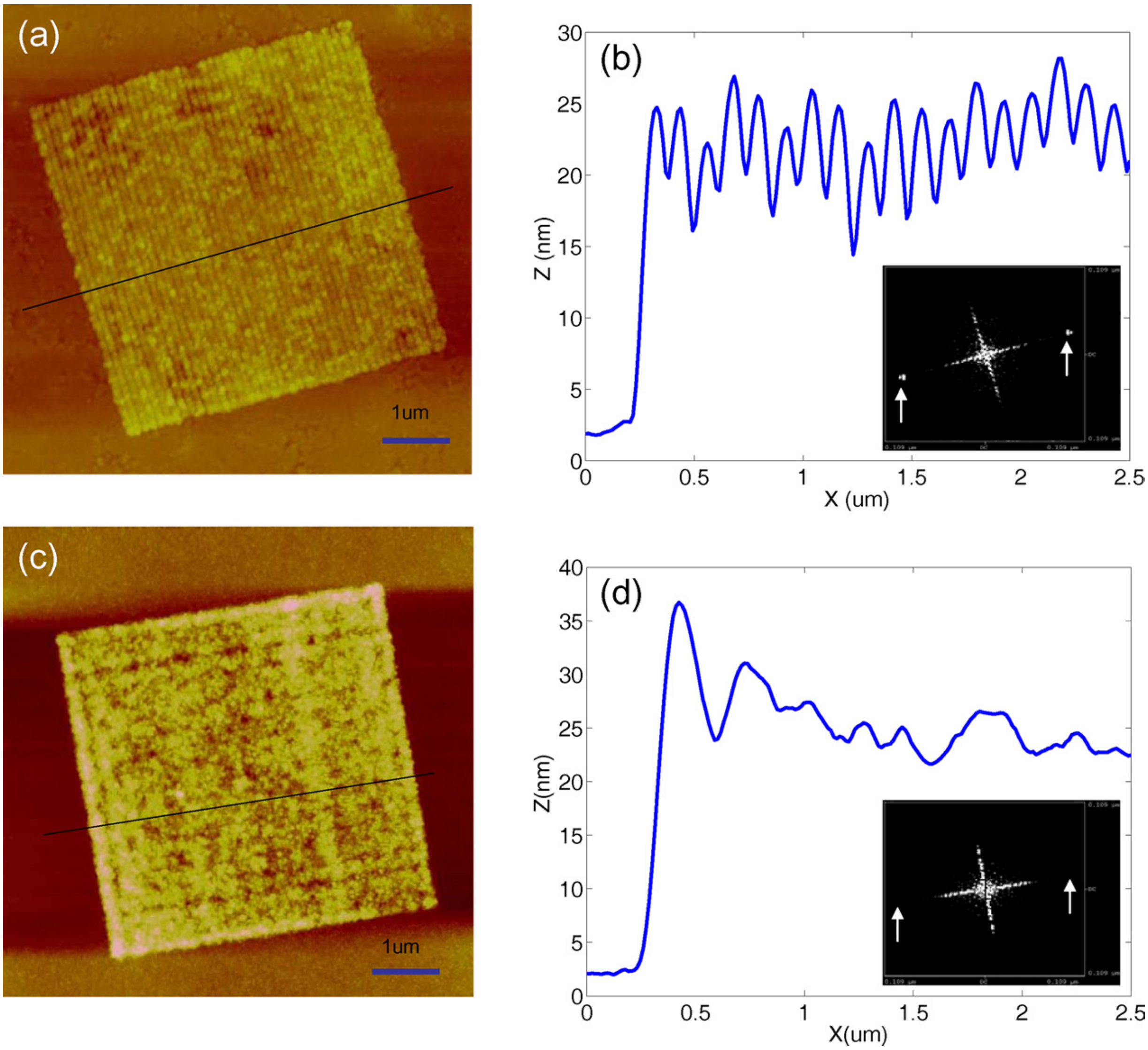

Figure 6. (a) The image of 120 nm period grating object recorded by superlensing, (b) its average cross-section, and two-dimensional Fourier analysis plot (inset). The 60 nm half-pitch object image is clearly resolved with 365 nm incident light demonstrating $\lambda_0/6$ resolution. (c) The image of the same grating object recorded in control experiment, (d) its average cross-section and two-dimensional Fourier analysis plot (inset). As expected, without a superlens, the evanescent wave decayed beyond recovery and the sub-wavelength object was not recorded [23]. (Colour scale of (a) and (c): 0–100 nm).

4. Results and discussion

The superlens imaging results show that the nanowire object with 120 nm period is clearly resolved (figure 6(a)). The height modulation of the recorded image is easily observed in the cross-section plot (figure 6(b)) and the Fourier analysis showing sharp peaks of 126 ± 7 nm (figure 6(b) inset) further confirms that the imaged period is indeed that of the object. These results are strong indications that the evanescent field of the object is restored and recorded as an image by superlensing. With our design, a 60 nm half-pitch object has been successfully imaged with $\lambda_0 = 365$ nm illumination wavelength at $\lambda_0/6$ resolution, which is well beyond the diffraction limit.

Although it is clear that the object information has indeed been recovered on the silver surface, it is not as perfect as the original object image (figure 5(a)). Higher Fourier components decayed faster and could not be restored. Also, non-ideal chemical processes of photolithography and the surface roughness of the silver may have caused the non-uniformity of the image. The peak to valley is approximated to be ∼7 nm from the cross-section profile (figure 6(b)) while the entire height of the developed feature is ∼30 nm. Several factors may have contributed to this. AFM tip convolution could result in shallow valleys, as the tip has finite size and taper. From the simulation result shown in figure 4(c), a flatter field profile close to the silver surface may have contributed to the exposure of the residual layer. The line widening of the resist is another possible cause as negative resist tends to swell during baking and development processes. SP scattering on silver surface is also a potential source of noise which is discussed later in the section. Another factor in the imperfectness of the recorded image is the finite thickness of PR. Additional simulation studies for different resist thicknesses show small variations in the final E-field intensity profile; thinner PR can broaden the field. Further studies are needed on this subject.

The control experiment result evidently supports the role of silver as a superlens. Without the silver layer, no image contrast is recorded (figure 6(c)) regardless of the optimization of the exposure and development processes. Its cross-section (figure 6(d)) and Fourier spectrum analysis (figure 6(d) inset) also show no evidences of periodic structure. As predicted in the numerical simulations, the evanescent wave generated by the object decayed significantly in the 75 nm thick PMMA layer. The decay length Z can be estimated by: $Z^{-1} = 4\pi\sqrt{a^{-2} - \varepsilon\lambda_0^{-2}}$, where a is the grating period, ε is the permittivity of surrounding media and λ_0 is the free space wavelength. Inside the dielectric medium, PMMA ($\varepsilon \sim 2.4$), evanescent waves $a = 120$ nm period will decay to approximately 1/3 of the original field within 11 nm above the object.

Imaging conditions were optimized for both the superlensing and control experiments to obtain the best contrast and have better control of reproducibility. These two experiments demonstrated that a well-designed silver layer indeed acts as a superlens that is capable of imaging well below the diffraction limit.

In order to verify that the results in figures 6(a) and (b) came from the predicted transfer function of the superlens (figure 2(d)), several objects with different periods have been imaged under the same exposure condition (figure 7). The wavenumbers represented by different periodic objects are indicated by black arrows in the transfer function curve in figure 2(d), which shows that the transmission intensity decreases for larger periods. The imaging results show good agreement with the calculation in figure 2(d). The 140 nm period image was recorded with good fidelity (figure 7(b)) as the cross-section shows clear periodic modulation (figure 7(e)). Lower image contrasts are shown for 100, 160 and 180 nm period objects (figures 7(a), (c) and (d), respectively).

A new imaging result, presented in figure 7(a), shows further improved resolution of $\lambda_0/7$ with the recorded image of a 50 nm half-pitch grating object. The same exposure and development conditions were used as that of the 120 nm grating images. Figure 8(f) is the AFM image of the developed features recorded by PR. As discussed earlier, even though the image is not perfect

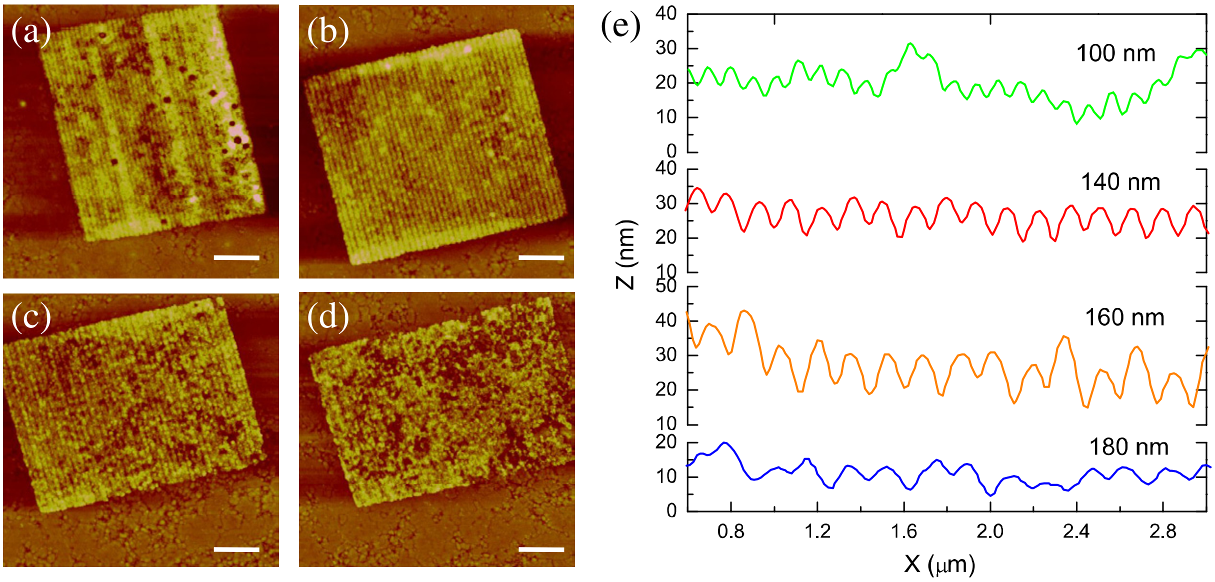

Figure 7. Experimental verification of optical transfer function of the superlens. Images of grating objects with periods (a) 100 nm, (b) 140 nm, (c) 160 nm, and (d) 180 nm recorded by the superlens structure. AFM image of 100 nm period grating recorded through superlens imaging (a) clearly show the periodic pattern, a resolution of $\lambda_0/7$. Scale bars represent 1 μm. (e) Average cross-sections of developed images. The exposure condition is kept the same with that of 120 nm images in figure 6(a). 140 nm object is imaged also with clear contrast while the transmissivity decreases for 100, 160 and 180 nm periodic objects. This is in good agreement with the trend of transmissivity for each period indicated in the transfer function (figure 2(d)). (Colour scale of (a)–(d): 0–100 nm).

due to various surface defects and non-ideal imaging conditions, the imaging of a 100 nm period object is another strong evidence of superlensing by silver.

In addition to periodic gratings, an arbitrary object (‘NANO’) was also imaged with a line width of 40 nm. Exposure and development conditions were also optimized for the best imaging result. The grating objects represent a very narrow band of wavenumbers, but an object such as the word ‘NANO’ has broadband Fourier components. Figure 8(a) is the focused ion beam image of the object. The image captured by the superlens (figure 8(b)) clearly shows far better resolution with a line width of 90 nm (figure 8(d)), while that of the control experiment (figure 8(c)) still resulted in diffraction-limited image with line width of 360 nm (figure 8(e)) which is comparable to the exposure wavelength (365 nm). A concern might be raised that longer development time might improve the resolution of the control image since the developer is known to attack the exposed part of the PR from all sides further reducing the line width. However, it was found experimentally that longer development does not reduce the line width, but mainly reduces the height of the developed features because the exposed region close to the surface is already fully cross-linked beyond the possibility of further development. The imaging of such arbitrary patterns proves that a wide band of large wave vectors are transmitted through the superlens, which enables sub-diffraction-limited imaging of an arbitrary pattern.

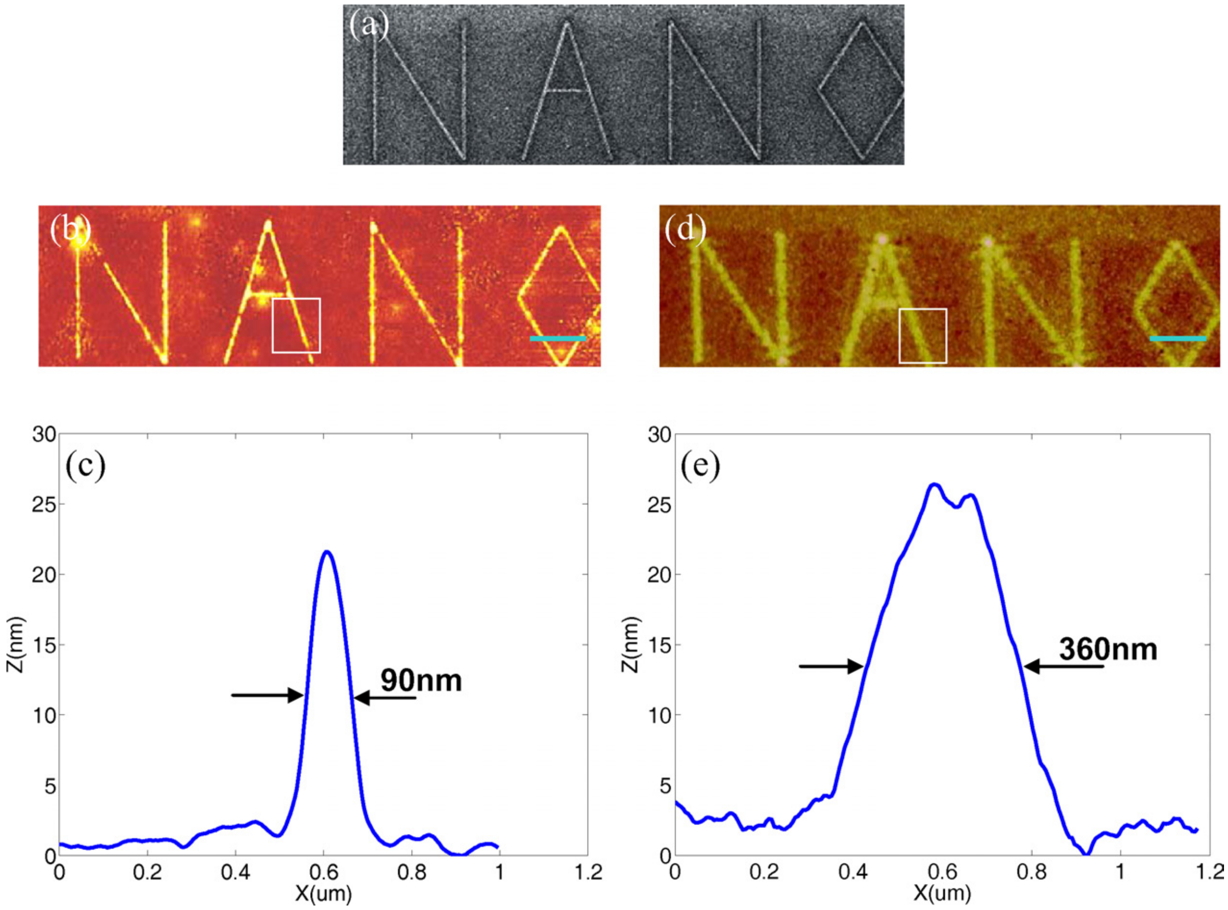

Figure 8. The imaging of a two-dimensional arbitrary object 'NANO'. (a) Focused Ion Beam (FIB) image of the object 'NANO' after fabrication on Cr film. (b) Superlensing image (scale bar 2 μm) and (c) its cross-section profile. (d) Control imaging result of the same object (scale bar 2 μm) and (e) its average line cross-section. Line width of ~90 nm is achieved with superlensing while the control imaging produced diffraction-limited image with line width ~360 nm. The average line widths were estimated from the zoomed-in images of indicated square window. (Colour scale of (b) and (d): 0–100 nm).

In order to demonstrate how the surface roughness of the superlens layer influences the performance of the superlens, figure 9 shows two imaging results on a silver surface with inhomogeneous surface quality. The RMS roughness of the silver surface indicated by white dashed circles had been measured to be 4–5 nm before the imaging experiment while smoother areas are 1–1.5 nm. Grating images are successfully recorded on smoother areas (figure 9(a)), while in rougher areas, the imaged lines are broken and no images are recorded at all. It is more evident in figure 9(b) where the bare silver surface roughness can be seen. An arbitrary object, the letter 'N' is partially recorded only on the smoother areas. The effect of surface imperfections on the superlens imaging becomes more severe when the features size becomes comparable to the size of the silver grains.

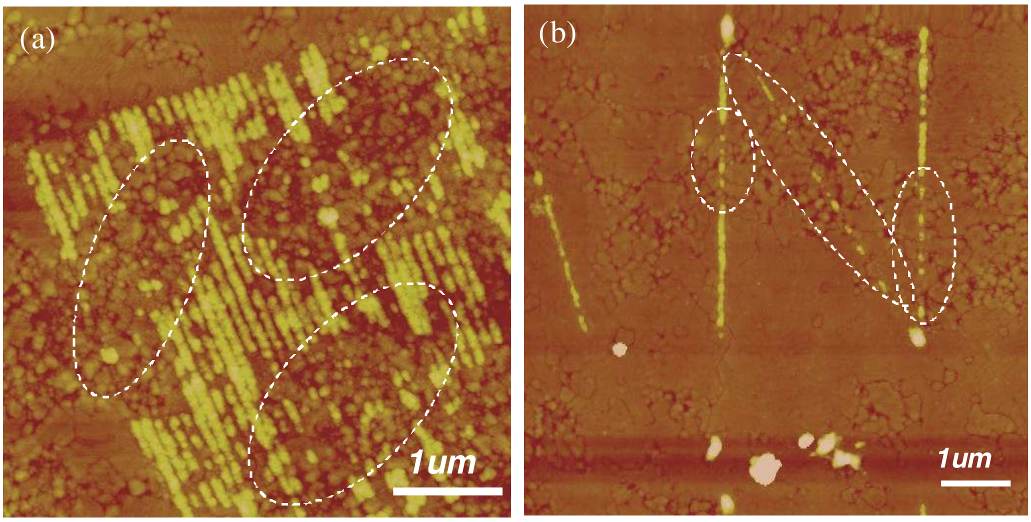

Figure 9. The effect of silver surface roughness on imaging quality. Developed images of (a) a grating object and (b) a letter object 'N' on surfaces with inhomogeneous roughness. The local roughness variation resulted in inconsistent imaging results within one object. White circles represent regions with silver surface roughness of 4–5 nm RMS where images failed to be recorded. Images are recorded on smoother areas with 1–2 nm RMS roughness. (Colour scale: 0–100 nm).

5. Conclusion

We presented experimental and theoretical investigations of the optical superlens using a thin slab of silver. Optical imaging with resolution well below the diffraction limit has been demonstrated. A 50 nm half-pitch periodic object has been successfully imaged using a superlens with 365 nm incident wavelength demonstrating $\lambda_0/7$ resolution. The imaging of an arbitrary two-dimensional object, 'NANO', with ∼40 nm line width confirmed that the superlens is capable of imaging arbitrary nanostructures with sub-diffraction-limited resolution. The optical superlens has a potentially significant impact in optics and imaging, medical sciences, and high-density memory devices.

Acknowledgments

The authors would like to thank Zhaowei Liu for helpful discussions. The authors acknowledge support from the Office of Naval Research (ONR)/Defense Advanced Research Projects Agency/Multidisciplinary University Research Initiative (MURI) (ONR grant N00014-01-1-0803), from NSF for the Center for Nanoscale Science and Engineering (grant DMI-0327077).

References

[1] Fischer U C and Zingsheim H P 1981 Sub-microscopic pattern replication with visible-light *J. Vac. Sci. Technol.* **19** 881–5

[2] Betzig E, Trautman J K, Harris T D, Weiner J S and Kostelak R L 1991 Breaking the diffraction barrier – optical microscopy on a nanometric scale *Science* **251** 1468–70

[3] Pendry J B 2000 Negative refraction makes a perfect lens *Phys. Rev. Lett.* **85** 3966–9

[4] Veselago V G 1968 Electrodynamics of substances with simultaneously negative values of sigma and mu *Sov. Phys.—Usp* **10** 509–14

[5] Shelby R A, Smith D R and Schultz S 2001 Experimental verification of a negative index of refraction *Science* **292** 77–9

[6] Yen T J, Padilla W J, Fang N, Vier D C, Smith D R, Pendry J B, Basov D N and Zhang X 2004 Terahertz magnetic response from artificial materials *Science* **303** 1494–6

[7] Wiltshire M C K, Pendry J B, Young I R, Larkman D J, Gilderdale D J and Hajnal J V 2001 Microstructured magnetic materials for rf flux guides in magnetic resonance imaging *Science* **291** 849–51

[8] Wiltshire M C K, Hajnal J V, Pendry J B, Edwards D J and Stevens C J 2003 Metamaterial endoscope for magnetic field transfer: Near field imaging with magnetic wires *Opt. Express* **11** 709–15

[9] Smith D R, Pendry J B and Wiltshire M C K 2004 Metamaterials and negative refractive index *Science* **305** 788–92

[10] Parazzoli C G, Greegor R B, Li K, Koltenbah B E C and Tanielian M 2003 Experimental verification and simulation of negative index of refraction using snell's law *Phys. Rev. Lett.* **90** 107401

[11] Linden S, Enkrich C, Wegener M, Zhou J F, Koschny T and Soukoutis C M 2004 Magnetic response of metamaterials at 100 terahertz *Science* **306** 1351–3

[12] Iyer A K, Kremer P C and Eleftheriades G V 2003 Experimental and theoretical verification of focusing in a large, periodically loaded transmission line negative refractive index metamaterial *Opt. Express* **11** 696–708

[13] Houck A A, Brock J B and Chuang I L 2003 Experimental observations of a left-handed material that obeys snell's law *Phys. Rev. Lett.* **90** 137401

[14] Grbic A and Eleftheriades G V 2004 Overcoming the diffraction limit with a planar left-handed transmission-line lens *Phys. Rev. Lett.* **92** 117403

[15] Smith D R, Schurig D, Rosenbluth M, Schultz S, Ramakrishna S A and Pendry J B 2003 Limitations on subdiffraction imaging with a negative refractive index slab *Appl. Phys. Lett.* **82** 1506–8

[16] Fang N and Zhang X 2003 Imaging properties of a metamaterial superlens *Appl. Phys. Lett.* **82** 161–3

[17] Blaikie R J and McNab S J 2002 Simulation study of 'perfect lenses' for near-field optical nanolithography *Microelectron. Eng.* **61–62** 97–103

[18] Johnson P B and Christy R W 1972 Optical-constants of noble-metals *Phys. Rev.* B **6** 4370–9

[19] Weber W H and Ford G W 1981 Optical electric-field enhancement at a metal-surface arising from surface-plasmon excitation *Opt. Lett.* **6** 122–4

[20] Raether H 1988 Surface-plasmons on smooth and rough surfaces and on gratings *Springer Tracts Mod. Phys.* **111** 1–133

[21] Liu Z W, Fang N, Yen T J and Zhang X 2003 Rapid growth of evanescent wave by a silver superlens *Appl. Phys. Lett.* **83** 5184–6

[22] Giannattasio A, Hooper I R and Barnes W L 2004 Transmission of light through thin silver films via surface plasmon-polaritons *Opt. Express* **12** 5881–6.

[23] Fang N, Lee H, Sun C and Zhang X 2005 Sub-diffraction-limited optical imaging with a silver superlens *Science* **308** 534–7

[24] Fang N, Liu Z W, Yen T J and Zhang X 2003 Regenerating evanescent waves from a silver superlens *Opt. Express* **11** 682–7

[25] Ramakrishna S A and Pendry J B 2002 The asymmetric lossy near-perfect lens *J. Mod. Opt.* **49** 1747–62

[26] Barnes W L, Dereux A and Ebbesen T W 2003 Surface plasmon subwavelength optics *Nature* **424** 824–30

[27] Melville D O S, Blaikie R J and Wolf C R 2004 Submicron imaging with a planar silver lens *Appl. Phys. Lett.* **84** 4403–5

[28] Stillwagon L E and Larson R G 1990 Leveling of thin-films over uneven substrates during spin coating *Phys. Fluids* A **2** 1937–44

[29] Smith D R 2005 How to build a superlens *Science* **308** 502–3